Passive Accelerometer Using Unstressed Patch Antenna Interrogated by FMCW Radar

Liyu Xie, *Member, IEEE*, Tonghai Wu, Zhuoran Yi, Xiaoli Fu, Wei Zang, and Wensheng Lu

***Abstract*—Conventional accelerometers rely on cables or batteries to transmit power and data, which has raised the possibility of failure and maintenance complications. However, antenna-based acceleration sensors can achieve wireless and passive sensing, while the cycling stress inside the vibration member will significantly influence the durability of the sensor in practical utilization. Based on the patch antenna with an overlapping subpatch, this study proposes an unstressed passive wireless accelerometer with a frequency-modulated-continuous-wave dynamic access. The sensing antenna of the proposed accelerometer is not affected by inertial forces, which effectively improves its usability and endurance for structural monitoring. A COMSOL-based simulation is conducted to verify the workability of the accelerometer's sensing node. The practical viability of the sensing node and wireless interrogation system is investigated via experiments. Furthermore, the shifts of the resonant frequency of the antenna sensor triggered by the change in total radiation length due to inertial forces are collected to obtain acceleration. Subsequently, the obtained results are compared to the theoretical value, with an average testing range error of 4.3%. Accordingly, this design provides a promising alternative for engineering requirements such as modal parameter identification due to its simple construction, optimal accuracy, and durability.**

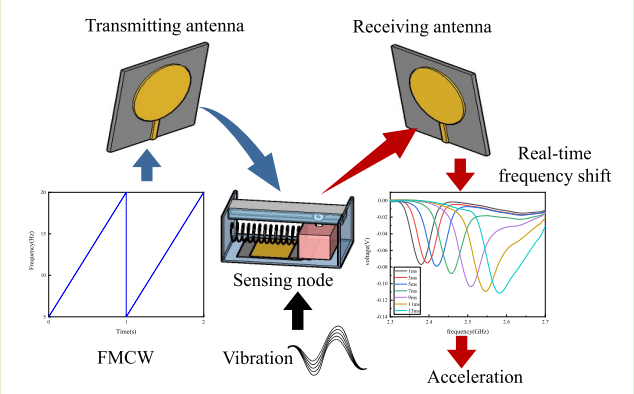

***Index Terms*— Acceleration sensor, frequency-modulated-continuous-wave (FMCW) radar, passive wireless, patch antenna.**

I. Introduction

AS THE global large-scale construction boom recedes, there is now a greater need to focus on the management, maintenance, and operation of aged buildings [1]. There is a demand for routine monitoring of some important performance of the structures to ensure the proper service of these structures [2]. The monitoring of acceleration parameters is remarkably noteworthy for vibration control [3], comfort-level control [4], and seismic response monitoring [5], especially for long-span structures [6] and towering structures [7].

Various accelerometers have been widely used in different areas over the years, including MEMS-based [8], capacitive [9], and piezoelectric accelerometers [10], and various novel accelerometers with better performance, such as higher sensitivity [11] and a larger measuring range [12], are being investigated simultaneously [13]. However, because most accelerometers still require cables for data transmission and energy supply, the installation of sensors incurs more difficulties and increases monitoring time and labor costs [14]. Moreover, the utilization of complex cables further increases the difficulties in troubleshooting and repairing the sensors.

Recently, wireless sensors have garnered considerable interest [15] in addressing the aforementioned cable limitations. However, most existing wireless sensors are implemented with a communication unit and internal memory, which still have to be replaced regularly due to the limited capacity of the battery [16]. One alternative to batteries is powering sensors with energy harvest technology. However, the energy harvested from ambient energy, such as solar power, ambient vibration, and radio frequency energy [17], still has a big gap with the required energy to feed sensors' operation [18]. In addition,

Manuscript received 24 February 2023; revised 29 May 2023; accepted 29 May 2023. Date of publication 14 June 2023; date of current version 1 August 2023. This work was supported in part by the National Natural Science Foundation of China under Grant 52078375 and Grant 52178298 and in part by the Top Discipline Plan of Shanghai Universities-Class I. The associate editor coordinating the review of this article and approving it for publication was Dr. Eui-Hyeok Yang. *(Corresponding author: Xiaoli Fu.)*

Liyu Xie, Tonghai Wu, Zhuoran Yi, and Wensheng Lu are with the Department of Disaster Mitigation for Structures, Tongji University, Shanghai 200092, China (e-mail: liyuxie@tongji.edu.cn; 2132252@tongji.edu.cn; yzr1997@tongji.edu.cn; wally@tongji.edu.cn).

Xiaoli Fu is with the Department of Hydraulic Engineering, Tongji University, Shanghai 200092, China (e-mail: xlfu@tongji.edu.cn).

Wei Zang is with the College of Architecture and Urban Planning, Tongji University, Shanghai 200092, China (e-mail: zang@tongji.edu.cn).

Digital Object Identifier 10.1109/JSEN.2023.3284401

another inevitable limitation of such integrated sensors is higher cost and worse reparability resulting from excessive integration of sensing nodes, making them more challenging to use widely.

The above limitations of active sensors can be alleviated by passive sensors that consume very little or no power [19], [20]. Common passive wireless sensing schemes available today include inductive coupling [21] and surface acoustic waves (SAWs) [22]. Recently, some experts have also proposed mechanical ratcheting mechanisms as passive wireless sensors [23], [24] that are incompetent to record real-time data. Antenna-based schemes are gradually drawing the attention of researchers due to their simple construction and usability [25]. When an antenna is operated as a sensing node, it performs two functions simultaneously: sensing and communicating. In terms of the antenna's sensing function, some electromagnetic parameters (resonant frequency, return loss, and so on) will change with the external environment, which can be designed to represent external physical quantities that need to be monitored. In terms of the antenna's communication function, an antenna can transmit the changed electromagnetic parameters by backscattering aroused by the interrogated wave. Hence, by reading out the backscattered signal from the antenna at the receiving terminal, the change in the electromagnetic parameters can be detected, and the physical quantity being monitored can be identified.

In summary, an antenna-based sensor can theoretically achieve passive wireless sensing while decreasing the complexity of the sensing node. Nowadays, antenna sensors have been extensively studied in civil engineering, and monitoring under laboratory conditions has been achieved, such as displacement sensor [26], strain sensor [27], [28] crack sensor [29], and shearing force sensor [30]. These antenna sensors mentioned above are connected to the structure, and the change of the monitoring data leads to the alteration of the monolithic antenna's size, further shifting the antenna's resonant frequency. Some experts take it a step further and propose antennas with additional parts for solving problems triggered by direct stretching [31], [32]. Instead of focusing on the stretched size of the antenna, the relative displacement between the antenna and the additional part can also act as the sensing unit. Nonetheless, because of the low sampling rate of interrogation methods, the sensors mentioned above can only perform quasi-static sensing and are incapable of dynamic sensing, such as acceleration sensing.

Frequency-modulated continuous wave (FMCW) provides a novel alternative for improving sampling rate and enables dynamic sensing with antenna sensors. The time-dependent resonant frequency can be determined by the sweeping frequency with periodic time. Yao et al. [33], [34] designed a dynamic wireless interrogator based on FMCW to monitor the vibratory strain in real time and then fabricated a compact antenna-sensor interrogator for pressure sensing.

Currently, Yi et al. [35] proposed a passive wireless acceleration sensing system that uses an FMCW radar to query a patch antenna-based sensor node. The sensing unit is a patch antenna coupled with a hanging-over cantilevered patch,

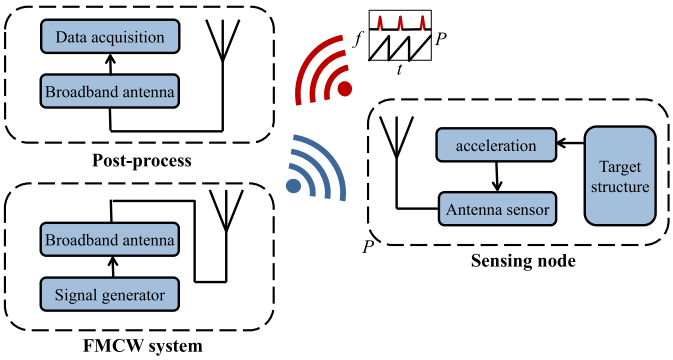

Fig. 1. Block diagram of wireless acceleration sensing system.

whose vibration would change the depth of the air gap between the radiation patch and the cantilevered one, resulting in the resonant frequency variation. Because the cantilevered patch oscillates in bending form in response to the acceleration magnitude, it can be categorized as a "direct deformation" sensing node. This will induce several problems, such as measurement error due to residual deformation after long-term use, fatigue damage, and material degradation of the cantilever.

This article presents a prototype of a "nondirect deformation" or unstressed acceleration sensing system that enables relatively high-sensitive acceleration measurement. The sensor comprises two parts: 1) a sensing node made up of a patch antenna and a mass-spring-damper system with a radiation patch attached under the proof mass and 2) an FMCW wireless interrogation system. The relative displacement of the proof mass due to the inertial forces will correspondingly make the radiation patch move and thus alter the total length of the combined radiation patch, further resulting in the shift of the resonant frequency. Then, the resonant frequency at each sampling is extracted using FMCW radar to calculate acceleration. This prototype provides a feasible method to measure acceleration with simple construction, good accuracy, and durability by avoiding the bending of a cantilevered patch, with a higher sampling rate of FMCW interrogation up to 500 Hz in this study. The sampling rate of FMCW interrogation can further reach kilohertz depending on the postprocess device.

II. Methodology

The acceleration sensing system has three parts: a sensing node, an FMCW interrogation system, and a data postprocessing part, as shown in Fig. 1. The workflow of this system is given as follows. The interrogation system generates FMCW and transmits it into space via a broadband antenna. Then, the FMCW is received by the antenna in the sensing node, which is connected to the target structure, and then reflected by the broadband antenna in the receiving terminal with the loss of the antenna in the sensing node. Finally, the signal carrying information about the antenna's resonant frequency and return loss is postprocessed, and the acceleration is calculated. The details of the first two parts will be covered minutely later in this section, and the operation of the data processing part will be shown in Section IV.

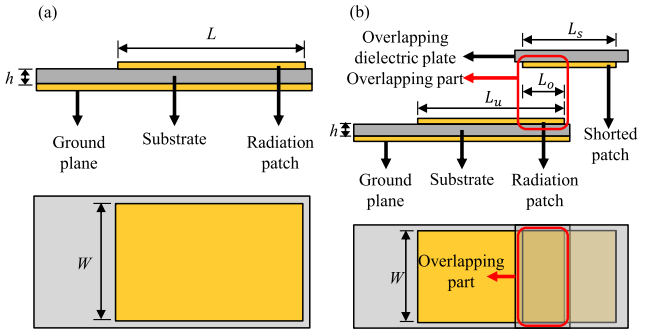

Fig. 2. Side and top views of antenna. (a) Regular patch antenna and (b) combined patch antenna.

A. Sensing Node

According to the cavity model theory, a patch antenna made up of a radiation patch and a ground plane can be treated as a resonant cavity. The cavity's resonant frequencies are proportional to the size of the radiation patch. The sensing node measures acceleration and transforms it into a form that the antenna's resonant frequency can identify. As the acceleration sensor node, a combined patch antenna is utilized in the design. A rectangular patch antenna plus an overlapping subpatch make up a combined patch antenna. The rectangular patch antenna comprises an upper radiating patch, a central dielectric plate, and a ground plane. The overlapping subpatch comprises an overlapping dielectric plate and a shorted patch, as shown in Fig. 2(a). The overlapping subpatch is placed over the rectangular patch antenna, and the electric current induced by interrogation waves can flow within the combined radiation patch. The two closely fit together to form the radiation unit.

Fig. 2(a) shows a typical rectangular patch antenna, where W and L are the size of radiation patch and h is the thickness of substrate. The resonant frequency of such a rectangular patch antenna can be expressed as

$$f_{\mathrm{mn}} = \frac{c}{2\sqrt{\varepsilon_e}}\sqrt{\left(\frac{m}{L_e}\right)^2 + \left(\frac{n}{W_e}\right)^2} \tag{1}$$

where m and n are the orders in longitudinal and transverse directions, respectively. Each set of m and n values represents a mode; c is the velocity of light; ε_e is the equivalent dielectric constant of the dielectric substrate, and L_e and W_e are the equivalent size of the patch antenna, which are larger than the physical dimension because of the fringe extensions. Because the antenna commonly operates in the TM10 mode, this sensing node is only affected by the length of the radiation patch. The resonant frequency in the longitudinal direction can be defined as

$$f_{10} = \frac{c}{2L_e\sqrt{\varepsilon_e}} \tag{2}$$

where ε_e and L_e can be calculated as

$$\varepsilon_e = \frac{\varepsilon_r + 1}{2} + \frac{\varepsilon_r - 1}{2}\left(1 + \frac{10h}{L}\right)^{-\frac{1}{2}} \tag{3}$$

$$L_e = L + 2\Delta L \tag{4}$$

where ε_r is the relative dielectric constant of the dielectric substrate and ΔL is the fringe extensions, which are obtained from

$$\Delta L = 0.412h\left(\frac{\varepsilon_e + 0.3}{\varepsilon_e - 0.258}\right)\left(\frac{W/h + 0.264}{W/h + 0.8}\right). \tag{5}$$

According to (3)–(5), ε_e and L_e are both related to h, and when the thickness of the substrate is much smaller than the physical dimension of the patch antenna, the fringe extensions can be neglected. Hence, the equation can be simplified as

$$f_{10} = \frac{c}{2L\sqrt{\varepsilon_r}}. \tag{6}$$

Similarly, the resonant frequency of the sensing node with combined radiation patches shown in Fig. 2(b) can be computed using (6)

$$L_{\mathrm{com}} = L_u + L_s - L_o \tag{7}$$

$$f = \frac{c}{2L_{\mathrm{com}}\sqrt{\varepsilon_r}} \tag{8}$$

where L_{com} is the length of the combined radiation patch in the resonant direction, f is the resonant frequency of the proposed acceleration sensor, L_u is the length of the radiation patch, L_s is the length of shorted patch, and L_o is the length of the overlapping subpatch and the closely fitting part between the radiation patch and the shorted patch. When the position of the overlapping subpatch changes relative to the rectangular patch antenna, the overlap length of the two shifts accordingly, and (7) can be rewritten as

$$L'_{\mathrm{com}} = L_u + L_s - L'_o + \Delta L \tag{9}$$

where L'_o is the initial length of overlapping and L'_{com} is the initial length of the combined radiation patch in the resonant direction.

From (8) and (9), the resonant frequency shifts when the overlapping subpatch is displaced relative to the rectangular patch antenna. Based on the above principles, the resonant frequency can be used to characterize the acceleration of the structure when the displacement of the overlapping subpatch is related to acceleration. Thus, a prototype of the sensing node capsulation technique based on the mass-spring-damper model is proposed to achieve the integration of acceleration. Fig. 3 shows a primitive sketch of the sensing node design.

For the model of the sensing node shown in Fig. 3(a), an overlapping subpatch is attached to the proof mass, which is suspended below the slide, and a spring is used to provide an elastic connection between the proof mass and the fixed end. It is appropriate to consider it approximately as a mass-spring-damper model. Assuming that the mass of the patch on the short is m, the stiffness of the spring is k, the friction damping of the slide is c, the instantaneous displacement of the frame vibration is x, and the relative displacement of the proof mass inside the accelerometer is z, then the equation of motion of the overlapping subpatch is expressed in the following equation:

$$m\ddot{z} + c\dot{z} + kz = -m\ddot{x}. \tag{10}$$

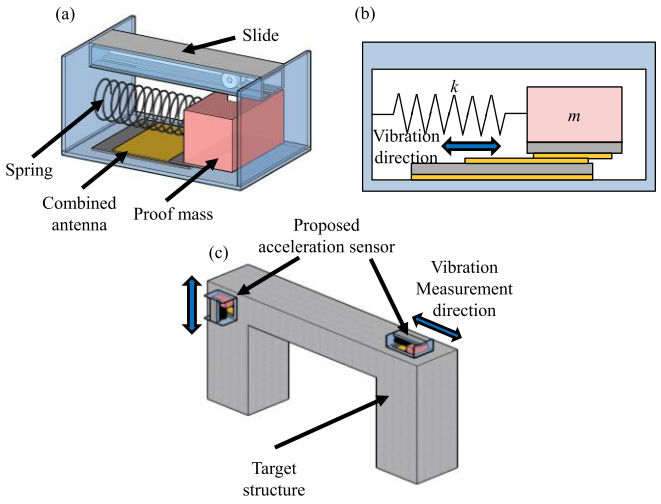

Fig. 3. Sensor design schematic. (a) Model of sensing node. (b) Design of sensing node. (c) Sensor installation.

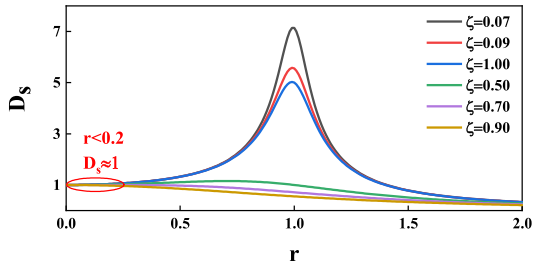

Fig. 4. Relationship between D_S, r, and ζ.

The target structure is assumed to carry out the harmonic vibration of the following equation:

$$x(t) = \mathrm{Im}\left(x_0 e^{i\Omega t}\right) \tag{11}$$

where x_0 is the harmonic vibration peak of the target structure and Ω is the natural frequency of the target structure. Substitute (11) into (10). Then, the relative displacement z can be calculated as

$$z = \frac{m}{k} D_s \ddot{x}_0 \sin(\Omega t - \alpha) + e^{-\zeta\omega_n t}\left(A_1 \cos\omega_d t + A_2 \sin\omega_d t\right) \tag{12}$$

where $\ddot{x}_0$ is the acceleration amplitude, ζ is the damping factor, α is the phase angle of the response hysteresis excitation obtained from $\tan\alpha = 2\zeta r/(1-r^2)$, r is the frequency ratio defined as $r = \Omega/\omega_n$, ω_n is the natural frequency of the sensing node. ω_d is the damped natural frequency defined as $\omega_d = \omega_n(1-\zeta^2)^{1/2}$; A_1 and A_2 are constants determined by initial conditions, and D_s is the frequency-response function whose expression is given as follows:

$$D_s = \frac{1}{\left[\left(1-r^2\right)^2 + (2\zeta r)^2\right]^{1/2}}. \tag{13}$$

According to (13), the relationship between D_s, r, and ζ is shown in Fig. 4.

For (12), the first term of the equation represents the forced vibration part of the total response. In contrast, the second term represents the intrinsic vibration, which can normally be neglected because it will decay to zero after a while due to damping. Thus, (12) can be simplified as

$$z = \frac{m}{k} D_s \ddot{x}_0 \sin(\Omega t - \alpha). \tag{14}$$

Because the sensor is connected to the structure, the change in the sensor's overlapping length ΔL equals the relative displacement z of the proof mass in the accelerometer

$$\Delta L = \frac{m}{k} D_s \ddot{x}_0 \sin(\Omega t - \alpha). \tag{15}$$

Hence, the relationship between f and $\ddot{x}$ can be deduced from the fact that ΔL is linear with $\ddot{x}$ when the value of the dynamic amplification factor D_s is constant at 1.

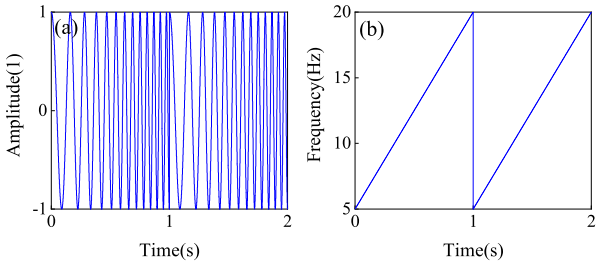

Fig. 5. Typical FMCW. (a) Time domain. (b) Time–frequency.

B. FMCW Interrogation System

FMCW is a modulated continuous wave whose main characteristic is that the frequency varies with time. One of the most common FMCW signals is linear FMCW, which can be seen as a chirp sweep signal that repeats over and over in the time domain and has been used for many applications in speed and distance measurement. In each period, the frequency of the FMCW signal shifts linearly from the sweep lower bound to the sweep upper bound. Fig. 5 shows the time-domain waveform and the time–frequency relationship of a typical sawtooth FMCW. In the example above, the starting frequency and off frequency are 5 and 20 Hz, respectively, and the repeated frequency is 1 Hz. The same is true at higher frequencies like kilohertz, where increasing the frequency is equivalent to increasing the sample rate for the proposed sensor.

To achieve wireless interrogation, an FMCW signal is broadcast to the antenna of the sensing node. The power flow of the incident FMCW wave can be expressed by (16) and Fig. 6

$$P_{in} = P_b + P_l + P_r \tag{16}$$

where P_{in} is the power of the incident wave, P_b is the power of backscattering, P_l is the power loss, and P_r is the power received by the receiving antenna. The portion of the FMCW wave whose frequency matches the resonant frequency will be received and reradiated by the antenna sensor. This process is called mode backscattering; it corresponds to the process represented by the red arrow in Fig. 6. In this "matching" moment, the P_r drops to its lowest position because the apex of the power transmits to the sensing node and P_b reaches the maximum. Hence, there is a crest that is not

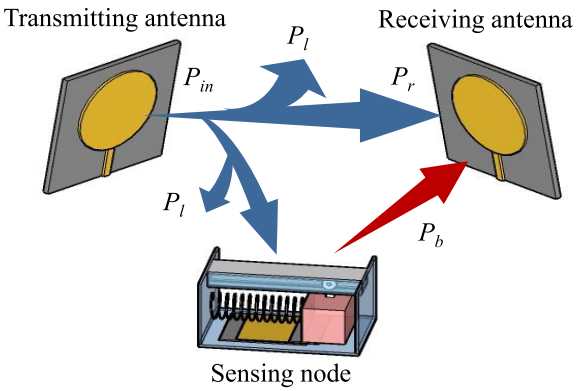

Fig. 6. Propagation process of FMCW waves.

in the original signal in each period of the signal received by the broadband antenna, which corresponds to the resonant frequency of this instance. As the subpatch position varies, the frequency corresponding to each period's trough also shifts.

The signal generation of the FMCW generally comprises signal generation, frequency modulation, and amplification modules. Generally, the signal generation module uses an oscillator to generate an alternating voltage signal by regulating the supply dc voltage through internal circuitry. A voltage-regulated oscillator (VCO) is typically used to refrequency the low-frequency alternating voltage signal to reach the gigahertz level. A voltage-controlled oscillator is an oscillation circuit in which the frequency of the output RF signal is controlled by the frequency of the input alternating voltage signal. The voltage-controlled oscillator generates a high-frequency RF signal when a low-frequency voltage is applied. Because the output power of the voltage-controlled oscillator is lost in one cycle, the output power must be boosted by an amplifier in the last.

III. Simulation in COMSOL

Section III provides the feasibility of the method proposed in Section II. First, the specific parameters of the prototype will be presented. Then, to verify that the link between acceleration and resonant frequency established by the prototype does exist and can be measured, multiphysics software COMSOL is used, and only the workability of the sensing node is considered in this section. The FMCW interrogation is tested in the next chapter. Finally, the broadband antenna accessing the antenna sensor and obtaining the key parameters will be simulated on HFSS software.

A. Setup of Parameters

This study's featured patch antenna works at around 2.4 GHz in the laboratory's available testing environment.

The length of the shorted patch L_s is fixed as being longer than the maximum range of variation in overlap length $\Delta L_{\max}$ to ensure that changes in the overlap length of the antenna do not affect its transceiver performance. Because of the limitation of modular VCO in the subsequent experiments, the overlap length $\Delta L_{\max}$ was set to 3 mm to keep the frequency variation of the combined patch within the VCO sweep range. This limitation can be resolved by replacing modular VCO with discrete VCO that allows for more flexible metrics.

TABLE I
Basic Parameters of Antenna Sensor

Parameters	L (mm)	W (mm)	L_u (mm)	L_s(mm)	L_g'(mm)
Value	52.5	49	26.6	18	6
Parameters	ΔL_{max} (mm)	ε_r	$\ddot{x}_0$(g)	m(g)	k(N/m)
Value	3	2.2	7.5	10	250

As for the capsulation of the sensing node, the range is the critical condition for parameter setting. The vibration of bridges and building structures in civil engineering, such as frame structures and frame shear structures, is generally low-frequency vibration with a first-order intrinsic frequency of several hertz [35]. Thus, the ideal upper operating frequency of the sensor f_{up} can be determined, that is, the operating range can cover the vibration frequency range of large civil engineering structures. Thus, a suitable operating frequency range is determined according to the actual engineering requirements.

Fig. 4 shows that when the frequency ratio is below 0.2, the value of the dynamic amplification factor D_s is approximately constant at 1, implying that the amplitude distortion of the acceleration measurement can be approximately neglected [36]. In this way, the upper operating frequency of the sensor can be obtained to be greater than the system's undamped inherent frequency ω_n

$$0.2\omega_n > 2\pi f_{\text{up}}. \tag{17}$$

After the inherent frequency ω_n is determined, the relationship between the mass of a block m and spring stiffness k can be calculated.

According to (14), the maximum range of the accelerometer to be designed can be determined as

$$\ddot{x}_0 = \frac{k\Delta L_{\max}}{m D_s}. \tag{18}$$

Thus, the settings for the sensing node are determined and listed in Table I, where g is the gravitational acceleration constant.

The ratio of the accelerometer frequency to the excitation frequency must be evaluated according to (17) to ensure that the frequency-response function converges to about 1. According to the parameters set above, the intrinsic frequency of the sensing node is shown as follows:

$$\omega_n = \sqrt{\frac{k}{m}} = 158 \text{ (rad/s)}. \tag{19}$$

The sensor's capsulation characteristics can be adjusted to fulfill the requirements for a given structure when used with a certain monitoring scope, which may have various operating frequencies, bandwidth, or range requirements for accelerometers.

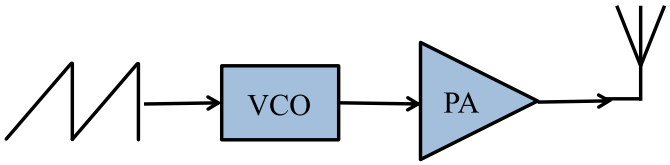

Fig. 7. Block diagram of FMCW radar.

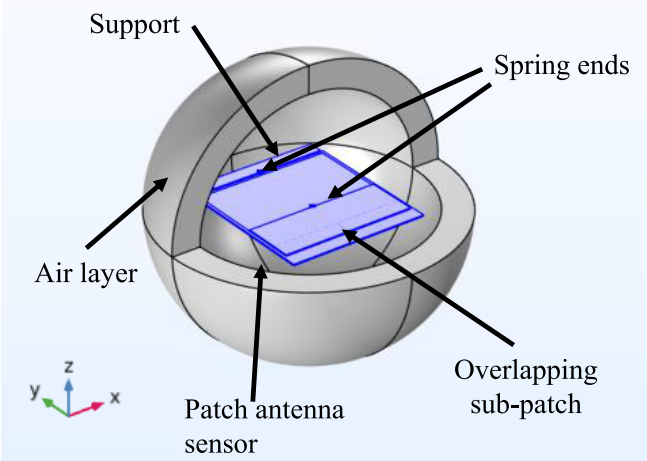

Fig. 8. Model in COMSOL MULTIPHYSICS.

B. Simulation Based on COMSOL

Fig. 8 shows the model. The subtract material and the overlapping subpatch were set to Rogers RO3003, whose dielectric constant is listed above. Perfect E was assumed for the boundary of the radiation patch and the upper surface of the cantilever beam, which represents a perfectly conducting surface. To account for the far-field effect, the entire sensor was housed inside an air ball that served as a radiation boundary. A lump port at the end of the feed line was used to excite the antenna sensor instead of plane wave excitation to make the simulation easier. The overlapping subpatch was connected to the support by a spring-loaded damper, which is not shown in the model. To imitate the state when the sensor was attached to the structure, the lower surface of this sensor and the fixed end of the spring were assumed to vibrate as a whole. The overlapping subpatch was set to perform rigid body translation in the y-direction only. To simulate the vibration of the target structure while reducing the modeling difficulty, the subpatch was added with additional mass for the proof mass, which can be modeled without it. The rectangular patch antenna and overlapping subpatch were set to frictionless contact to simulate a tight fit.

First, the relationship between displacement and acceleration was analyzed. Various accelerations were applied to the ground plane and support during the simulation. Fig. 9 represents the displacement of the proof mass, namely, the amount of overlap length variation, in relation to the acceleration.

The results of the simulation-based analysis of the sensing structure are compatible with the conclusions of the analysis of the mechanical model of the sensing mass block in that there is a linear relationship between the acceleration and displacement

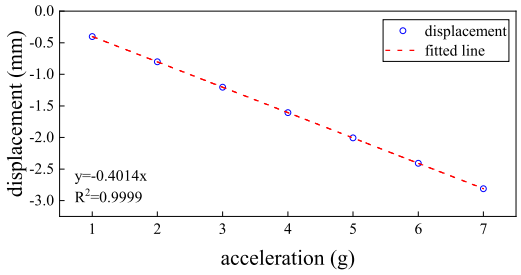

Fig. 9. Relationship between displacement and acceleration.

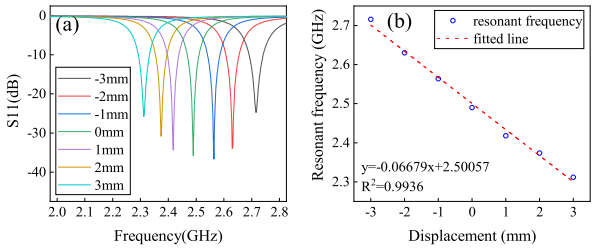

Fig. 10. (a) $S11$ curve and (b) fitting of resonant frequency and relative displacement.

of the sensing mass block, as shown in the following equation:

$$\Delta L(\text{mm}) = -0.4014a(\text{g}). \tag{20}$$

After confirming the linearity between displacement and acceleration, the resonant frequencies of the antenna under different overlap length variations (-3, -2, -1, 0, 1, 2, and 3 mm) are obtained in Fig. 10(a) to examine the viability of linearly representing acceleration. The antenna $S11$ curves are shown in Fig. 9 at various displacements, while Fig. 10(b) extracts the resonant frequency of each curve and fits it to the displacement.

According to Fig. 10, the connection between the resonant frequency of the antenna sensor and the subpatch's displacement can be fit as

$$f(\text{GHz}) = -0.06679\Delta L(\text{mm}) + 2.50057. \tag{21}$$

Fig. 10 generally shows a nearly linear relationship between the overlapped length and the resonant frequency. The fit line's correlation coefficient is 0.9936, demonstrating that the resonance frequency shifts linearly as the overlapped length increases. Combining (20) and (21), the transform equation for resonant frequency and acceleration is calculated in (22). As shown in the following equation, the proposed sensor is linear; hence, the slope of the fit line representing the theoretical sensitivity coefficient of the antenna sensor is 26.8 MHz/g:

$$f(\text{GHz}) = 0.0268a(\text{g}) + 2.5054. \tag{22}$$

The key metrics of the sensor model, such as the amplitude–frequency characteristic, can be analyzed with the transform equation. The amplitude–frequency curves of the system change in accordance with the change in structural damping, as shown in the analysis of the dynamic response of a damped single-degree-of-freedom system with structural dynamics. The amplitude–frequency curve's flat region is crucial for determining how helpful an accelerometer is. A simple

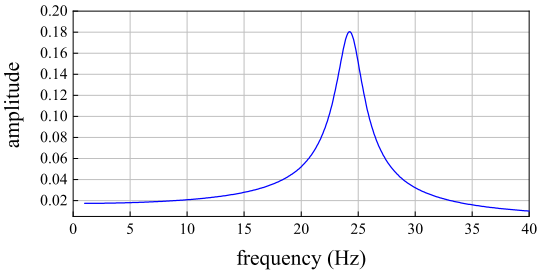

Fig. 11. Amplitude and frequency curve of the sensing node.

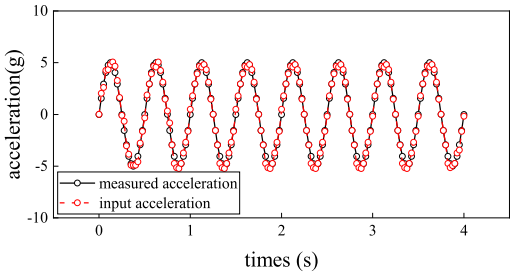

Fig. 12. Measurement of acceleration.

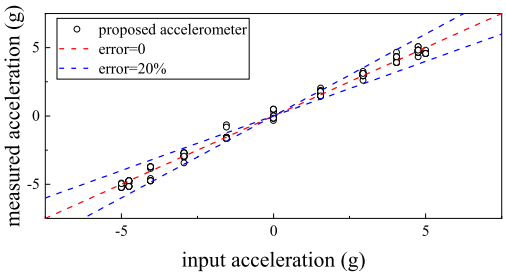

Fig. 13. Error of acceleration measurement.

harmonic waveform driving it at various frequencies is applied to the ground. The vibration amplitude of the proof mass was studied in the frequency domain of COMSOL, as shown in Fig. 11. The peak amplitude of vibration occurred at 24.3 Hz. Hence, the resonant frequency is 24.3 Hz, which is close to the calculated theoretical value. Fig. 11 shows that 0.5–10 Hz is the plateau of wavelength shift, and 10–24 Hz is a rapidly rising segment of wavelength change. The simulation showed that the working frequency range of the sensor is 0.5–10 Hz.

Then, the model was analyzed in the transient and frequency domains to determine the resonant frequencies at each moment to recreate the process of determining resonant frequencies in each cycle using FMCW. In the simulation, the time interval for transient analysis was set to 0.25 s, which corresponds to a repetition frequency of 40 Hz for FMCW, and the duration was set to 4 s. The minimum value of $S11$ at each moment was extracted, and the relationship between the resonant frequencies of the patch antenna at each moment was obtained.

As mentioned above, it was approximated that the resonant frequency is linearly related to acceleration. The acceleration response of the lower target structure was obtained by substituting the resonant frequency of each moment into (22), as shown in Fig. 10.

Figs. 12 and 13 show that this sensor model is sensitive and reliable for acceleration excitation, with insignificant amplitude differences and phase differences between the input and output waveforms and therefore has good measurement capability for structural vibration.

From the above simulation, it is clear that the acceleration can be calculated by measuring the resonance frequency and return loss in real time. However, because the feed line and lump port were used for interrogation rather than the FMCW radar, the simulation did not consider the effect of transmission and dissipation in free space. It can only exhibit a brief operating condition for the proposed accelerometer. Thus, more practical testing is required to confirm the viability, particularly for wireless interrogation.

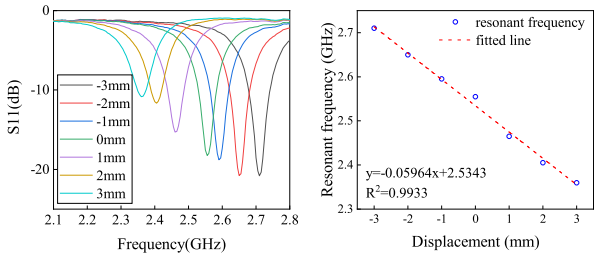

Fig. 14. Calibration of antenna sensor. (a) $S11$ curve and (b) relationship between displacement and resonant frequency during calibration.

IV. Experiment

In this section, the performance of the monitoring node and the passive wireless monitoring system via FMCW were tested by monitoring the displacement of the free vibration of the proof mass. When the proof mass performs free vibration, the frequency remains the same, and the value of its frequency-response function remains the same such that the displacement and acceleration remain in the same proportion at each moment, according to (15). Therefore, the displacement test can more easily characterize the results of acceleration tests.

A. Calibration

Because the ideal settings in the simulation were different from the actual experimental environment, the sensor must be calibrated in accordance with the procedures in Section III before resuming the experiment. This requires obtaining the conversion equation under the actual conditions. First, the sensor calibration was performed by obtaining the resonant frequency of seven states, which is identical to the simulation described previously. The $S11$ curves were examined by a vector network analyzer (VNA) in this section with maximum and minimum displacement set to 3 mm.

Due to the dimensional error of antenna fabrication and the imperfect short contact of the combined patch, the resonant frequency obtained by the VNA test is different from the simulation result, and the transform equation needs to be recalibrated according to the actual measurement result

$$f\,(\mathrm{GHz}) = -0.05964\Delta L\,(\mathrm{mm}) + 2.5343. \tag{23}$$

Fig. 14(a) shows the $S11$ curves, whereas Fig. 14(b) shows the displacement–resonant frequency relationship. Equation

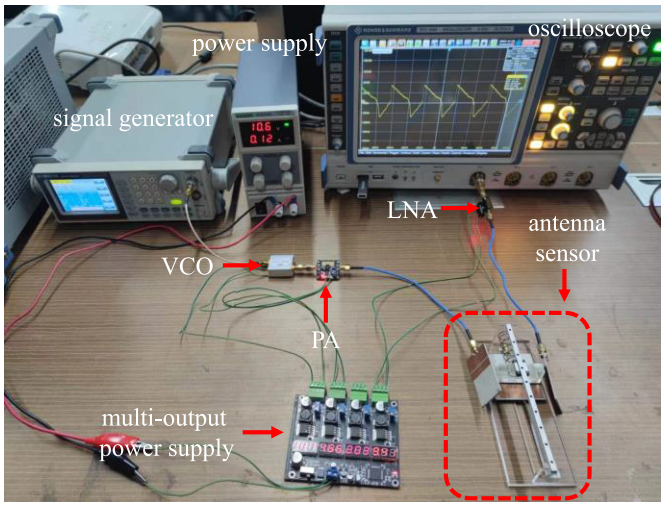

Fig. 15. Test system setup for the experiment.

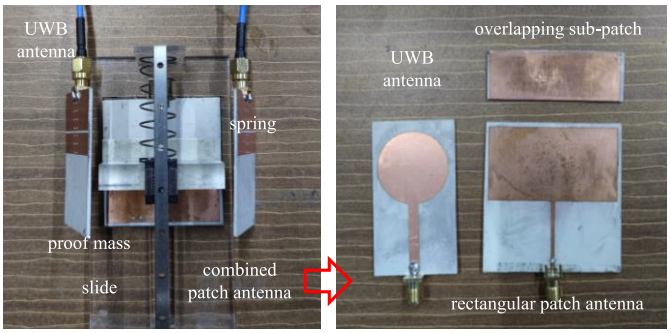

Fig. 16. Proposed passive wireless sensing node.

(23) shows the fit equation for the resonant frequency and displacement. The resonant frequency will rise linearly as displacement falls, just like in the simulation. These two associations have linear fitting coefficients higher than 0.99, indicating viability for the suggested sensing node.

B. Setup

The testing device is established and shown in Figs. 15 and 16. The experimental object had three main parts, as shown in Fig. 1. Copper was chosen as the component for the radiation patches on the manufactured sensors. The substrate of the rectangular patch antenna and the substrate for the subpatch were both considered Rogers RO3003. For the 0–4.5-V sawtooth signal generated by the signal generator, the frequency range of the voltage-controlled oscillator output in the FMCW is 2.3–2.72 GHz, and the amplifier connected to it was rated to operate in the frequency range of 1 M–3 GHz with a maximum gain of 20 dB in the frequency range. The FMCW is transmitted by the emitting antenna to the antenna sensor and then caught by the receiving antenna. The RTO1044 oscilloscope is used directly as a data collector to simplify the experiment setup. For practical applications, an analog-to-digital converter (ADC) can be used in place of the oscilloscope. The transmitted power is measured at 6.6 dbm by connecting the VCO with spectrum analyzer. In this experiment, the distance between the antenna sensor, emitting antenna, and receiving antenna was restricted to 3 cm

TABLE II
BASIC PARAMETERS OF VIBRATION

Parameters	T (ms)	ζ (1)	A (mm)
Value	50	0.15	3.0

TABLE III
BASIC PARAMETERS OF FMCW RADAR

Parameters	T_s (s)	f_s (Hz)	f_{low} (GHz)	f_{up} (GHz)
Value	1	500	2.30	2.72

because the signal's power was insufficient for long-distance transmission in free space. The power amplifier set in this system may be improved to quickly increase the interrogating distance.

C. Result

Because acceleration was proportional to displacement, the vibration of the proof mass was tested to ensure the viability of the proposed sensing node and wireless interrogation system. The initial displacement was applied to the proof mass to induce vibration, which was set to be the maximum variation in overlap length. As mentioned above, the sensing node can be regarded as a mass-spring-damper model. Slow-motion photography was used to record the movement of the proof mass, which is approximately harmonic. The proof mass trembled twice in 0.1 s, and the amplitude decreased from 3.0 to 1.2 mm after a cycle. Then, the period T, damping rate ζ, and frequency ω were calculated based on the following equations:

$$T_d = 2\pi/\omega_d = 0.1/2 = 50(\text{ms}) \tag{24}$$

$$e^{\zeta\omega_n T_d} = 3/1.2. \tag{25}$$

The basic parameters for the vibration were then solved and listed in Table II.

Equation (25) was then used to compute the proof mass' anticipated displacement $x(t)$

$$x(t) = Ae^{-\zeta\omega_n t}\cos(\omega_f t). \tag{26}$$

The basic parameters of the FMCW radar are then listed in Table III, where T_s is the sampling time for the radar and f_s is the repeated frequency of FMCW, which corresponds to the sampling frequency of the system. f_{up} and f_{low} are the uplink and downlink frequencies of FMCW, respectively, which correspond to the interrogating range of FMCW radar.

Backscattered signals were obtained from access patch antennas via receiving antennas, and the original echo signal waveform acquired from the oscilloscope is shown in Fig. 17. Here, the voltage amplitude of the signal can be taken to characterize the power of the signal.

Each echo signal was truncated and superimposed to produce separate time-domain signals. The time and frequency were also regarded as linear because the frequency is linear with the input control voltage, and the input control voltage is linear with the time. Thus, after converting the x-label directly into frequency coordinates whose range corresponds to f_{up}

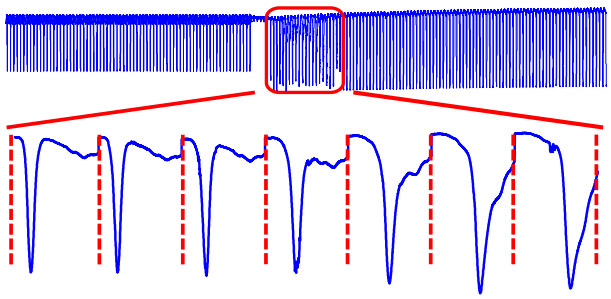

Fig. 17. Original signal obtained on the oscilloscope.

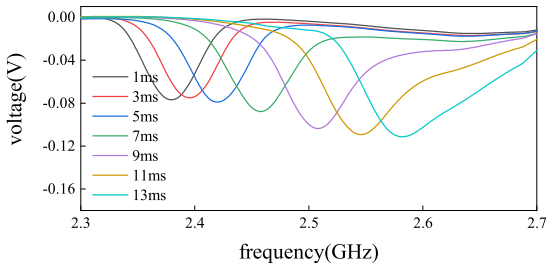

Fig. 18. Relationship between voltage (V) and frequency (GHz) at different moments.

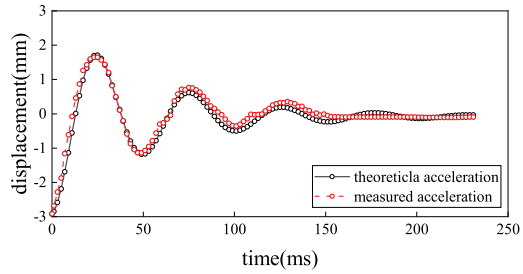

Fig. 19. Measured displacement using obtained resonant frequency.

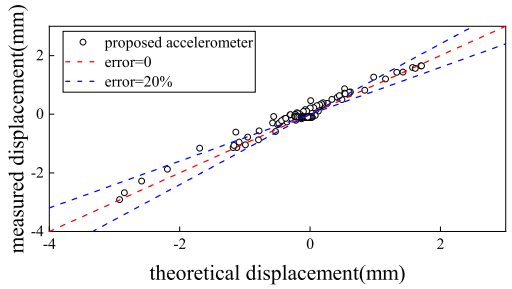

Fig. 20. Error of the proposed methods for vibrated displacement.

and f_{low}, the echo signals integrated and smoothed are plotted in Fig. 17.

The frequency corresponding to the lowest point of the echo signal curve at each moment in Fig. 18 is the resonant frequency of the combined antenna at that moment, and displacement is calculated based on (23), according to the resonant frequency obtained above. The result is shown in Fig. 19 and is compared to the theoretical free vibrations using the parameters stated in Table II. Then, the error is shown in Fig. 20.

A good fit between the measuring data and theoretical data in the first three cycles of free vibration was demonstrated by the results in Fig. 20. The error of the first three cycles' data was probably caused by: 1) environmental interference; 2) nontight contact of combined patches; and 3) unevenness of VCO tuning sensitivity. Also, the measured displacement tended to be constant after the third cycle, which is inconsistent with the theoretical acceleration. The cause of this difference is most likely the premature cessation of vibration of the mass due to friction. The test's overall average displacement error is 0.1273 mm, and the corresponding measuring range for the displacement variation is ±3.0 mm.

This measuring error can be equated with the acceleration error and is less than 4.3% compared to the measuring range, demonstrating the acceptable viability of the proposed sensing method.

TABLE IV
COMPARISON BETWEEN THE PROPOSED SENSOR AND THE RECENTLY DESIGNS

Type	Ref.	Range (g)	Sensitivity	Error (%)	Merit
Traditional Accelerometer	[38]	0-8g	1024 LSB/g	2.1	Small footprint
Micromechanical sensor	[24]	1.9-9.7 g	8.4 steps/g	-	Purely micromechanical
Antenna sensor	[35]	0-5g	0.3 MHz/g	4.5	Passive wireless
Antenna sensor	This work	0-7.5g	26.8 MHz/g	4.3	Unstressed passive wireless

A comparison of the proposed sensor with other accelerometers is given in Table IV. The comprehensive performance of the proposed sensors is still competitive with previous work, which also features passive wireless and improves durability through unstressed design.

V. CONCLUSION

A passive patch antenna sensing device was presented to measure the structure's acceleration. The acceleration-sensitive unit was designed to be separated from the antenna to prevent issues brought on by prolonged use. Hence, the antenna is not vulnerable to external forces while sensing. The displacement of the proof mass in the node can be sensed using the resonant frequency shift of a constructed patch antenna sensing node, further reflecting the acceleration of the attached structure. An equivalent model based on structural dynamics and a simulated model in COMSOL was used to confirm the design availability. Simulated and estimated linear relationships exist between the resonant frequency and structural acceleration. Its sensitivity in the needed frequency region has low distortion and good flatness. An experiment was conducted to measure the displacement of the proof mass in the sensing node to confirm the wireless feasibility further. The basic properties of the sensor node were used to set the parameters of FMCW radar, which was subsequently used for wireless measurement. The measured data using resonant frequency showed an average error rate for acceleration detection within 4.3%, showing great viability for the suggested sensing system.

REFERENCES

[1] J. M. W. Brownjohn, "Structural health monitoring of civil infrastructure," *Phil. Trans. Roy. Soc. A, Math., Phys. Eng. Sci.*, vol. 365, no. 1851, pp. 589–622, Feb. 2007, doi: 10.1098/rsta.2006.1925.

[2] T.-H. Yi, H.-B. Huang, and H.-N. Li, "Development of sensor validation methodologies for structural health monitoring: A comprehensive review," *Measurement*, vol. 109, pp. 200–214, Oct. 2017, doi: 10.1016/j.measurement.2017.05.064.

[3] T. Li, J. Guo, Y. Tan, and Z. Zhou, "Recent advances and tendency in fiber Bragg grating-based vibration sensor: A review," *IEEE Sensors J.*, vol. 20, no. 20, pp. 12074–12087, Oct. 2020, doi: 10.1109/JSEN.2020.3000257.

[4] S. Živanović, A. Pavic, and P. Reynolds, "Vibration serviceability of footbridges under human-induced excitation: A literature review," *J. Sound Vib.*, vol. 279, nos. 1–2, pp. 1–74, Jan. 2005, doi: 10.1016/j.jsv.2004.01.019.

[5] E. Cochran, J. Lawrence, C. Christensen, and A. Chung, "A novel strong-motion seismic network for community participation in earthquake monitoring," *IEEE Instrum., Meas. Mag.*, vol. 12, no. 6, pp. 8–15, Dec. 2009, doi: 10.1109/MIM.2009.5338255.

[6] Y. H. Zhang, Q. S. Li, J. H. Lin, and F. W. Williams, "Random vibration analysis of long-span structures subjected to spatially varying ground motions," *Soil Dyn. Earthq. Eng.*, vol. 29, no. 4, pp. 620–629, Apr. 2009, doi: 10.1016/j.soildyn.2008.06.007.

[7] Y. Q. Ni, Y. Xia, W. Y. Liao, and J. M. Ko, "Technology innovation in developing the structural health monitoring system for Guangzhou new TV tower," *Struct. Control Health Monit.*, vol. 16, no. 1, pp. 73–98, Feb. 2009, doi: 10.1002/stc.303.

[8] S. Finkbeiner, "MEMS for automotive and consumer electronics," in *Proc. Eur. Solid-State Device Res. Conf. (ESSDERC)*, Sep. 2013, pp. 9–14, doi: 10.1109/ESSCIRC.2013.6649059.

[9] M. Benmessaoud and M. M. Nasreddine, "Optimization of MEMS capacitive accelerometer," *Microsyst. Technol.*, vol. 19, no. 5, pp. 713–720, May 2013, doi: 10.1007/s00542-013-1741-z.

[10] G.-J. Lee, W.-J. Hwang, J.-J. Park, and M.-K. Lee, "Study of sensitive parameters on the sensor performance of a compression-type piezoelectric accelerometer based on the meta-model," *Energies*, vol. 12, no. 7, p. 1381, Apr. 2019, doi: 10.3390/en12071381.

[11] L. Qian and D. Li, "Use of magnetic fluid in accelerometers," *J. Sensors*, vol. 2014, pp. 1–9, Dec. 2014, doi: 10.1155/2014/375623.

[12] V. Narasimhan, H. Li, and M. Jianmin, "Micromachined high-g accelerometers: A review," *J. Micromech. Microeng.*, vol. 25, no. 3, Mar. 2015, Art. no. 033001, doi: 10.1088/0960-1317/25/3/033001.

[13] W. Babatain, S. Bhattacharjee, A. M. Hussain, and M. M. Hussain, "Acceleration sensors: Sensing mechanisms, emerging fabrication strategies, materials, and applications," *ACS Appl. Electron. Mater.*, vol. 3, no. 2, pp. 504–531, Feb. 2021, doi: 10.1021/acsaelm.0c00746.

[14] K. M. Z. Shams and M. Ali, "Wireless power transmission to a buried sensor in concrete," *IEEE Sensors J.*, vol. 7, no. 12, pp. 1573–1577, Dec. 2007, doi: 10.1109/JSEN.2007.908230.

[15] *Risk Monitoring of Buildings With Wireless Sensor Networks*. Accessed: Apr. 10, 2022. [Online]. Available: https://onlinelibrary.wiley.com/doi/epdf/10.1002/stc.73

[16] M. Abdulkarem, K. Samsudin, F. Z. Rokhani, and M. F. A. Rasid, "Wireless sensor network for structural health monitoring: A contemporary review of technologies, challenges, and future direction," *Struct. Health Monit.*, vol. 19, no. 3, pp. 693–735, May 2020, doi: 10.1177/1475921719854528.

[17] Y. Bai, H. Jantunen, and J. Juuti, "Energy harvesting research: The road from single source to multisource," *Adv. Mater.*, vol. 30, no. 34, Aug. 2018, Art. no. 1707271, doi: 10.1002/adma.201707271.

[18] R. Hidalgo-Leon et al., "Powering nodes of wireless sensor networks with energy harvesters for intelligent buildings: A review," *Energy Rep.*, vol. 8, pp. 3809–3826, Nov. 2022, doi: 10.1016/j.egyr.2022.02.280.

[19] D. Gould, M. Meiners, W. Benecke, and W. Lang, "Condensation detection using a wirelessly powered RF-temperature sensor," *IEEE Trans. Veh. Technol.*, vol. 58, no. 4, pp. 1667–1672, May 2009, doi: 10.1109/TVT.2008.2003258.

[20] H. Kou, Q. Tan, L. Zhang, H. Dong, J. Xiong, and W. Zhang, "Highly sensitive air-filled substrate integrated waveguide resonator integrated wireless passive slot-antenna for confined environmental detection," *IEEE Sensors J.*, vol. 19, no. 21, pp. 10027–10033, Nov. 2019, doi: 10.1109/JSEN.2019.2921148.

[21] M. T. P. Silva and F. H. Vasconcelos, "Temperature sensing system with short-range wireless sensor based on inductive coupling," *IEEE Sensors J.*, vol. 11, no. 10, pp. 2469–2478, Oct. 2011, doi: 10.1109/JSEN.2011.2140394.

[22] R. Stoney, D. Geraghty, and G. E. O'Donnell, "Characterization of differentially measured strain using passive wireless surface acoustic wave (SAW) strain sensors," *IEEE Sensors J.*, vol. 14, no. 3, pp. 722–728, Mar. 2014, doi: 10.1109/JSEN.2013.2285722.

[23] S.-Y. Wu, C.-Y. Hung, and W. Hsu, "A wirelessly readable and resettable shock recorder through the integration of LC circuits and MEMS devices," *Smart Mater. Struct.*, vol. 23, no. 9, Sep. 2014, Art. no. 095030, doi: 10.1088/0964-1726/23/9/095030.

[24] P. Schmitt and M. Hoffmann, "A passive acceleration sensor with mechanical 6 bit memory and mechanical analog-to-digital converter," *Micro Nano Eng.*, vol. 15, Jun. 2022, Art. no. 100142, doi: 10.1016/j.mne.2022.100142.

[25] K. M. Gee, P. Anandarajah, and D. Collins, "A review of chipless remote sensing solutions based on RFID technology," *Sensors*, vol. 19, no. 22, p. 4829, Nov. 2019, doi: 10.3390/s19224829.

[26] S. Xue, Z. Yi, L. Xie, G. Wan, and T. Ding, "A displacement sensor based on a normal mode helical antenna," *Sensors*, vol. 19, no. 17, p. 3767, Aug. 2019, doi: 10.3390/s19173767.

[27] Y. Hew, S. Deshmukh, and H. Huang, "A wireless strain sensor consumes less than 10 mW," *Smart Mater. Struct.*, vol. 20, no. 10, Oct. 2011, Art. no. 105032, doi: 10.1088/0964-1726/20/10/105032.

[28] L. Chen, L. Liu, L. Kang, Z. Wan, G. Wan, and L. Xie, "A multibranch U-shaped tunable encoding chipless RFID strain sensor for IoT sensing system," *IEEE Internet Things J.*, vol. 10, no. 6, pp. 5304–5320, Mar. 2023, doi: 10.1109/JIOT.2022.3221938.

[29] X. Xu and H. Huang, "Multiplexing wireless antenna sensors for crack growth monitoring," *Proc. SPIE*, vol. 7981, Mar. 2011, Art. no. 798144, doi: 10.1117/12.880688.

[30] I. Mohammad and H. Huang, "Shear sensing based on a microstrip patch antenna," *Meas. Sci. Technol.*, vol. 23, no. 10, Oct. 2012, Art. no. 105705, doi: 10.1088/0957-0233/23/10/105705.

[31] S. Xue, X. Li, L. Xie, Z. Yi, and G. Wan, "A bolt loosening detection method based on patch antenna with overlapping sub-patch," *Struct. Health Monit.*, vol. 21, no. 5, pp. 2231–2243, Dec. 2021, doi: 10.1177/14759217211055613.

[32] C. Wan, Z. Zheng, S. Xue, L. Xie, and G. Wan, "An angle sensor based on a sector ring patch antenna for bolt loosening detection," *Smart Mater. Struct.*, vol. 31, no. 4, Apr. 2022, Art. no. 045009, doi: 10.1088/1361-665X/ac55d9.

[33] J. Yao, S. Tjuatja, and H. Huang, "Real-time vibratory strain sensing using passive wireless antenna sensor," *IEEE Sensors J.*, vol. 15, no. 8, pp. 4338–4345, Aug. 2015, doi: 10.1109/JSEN.2015.2416672.

[34] J. Yao, S. Tjuatja, and H. Huang, "A compact FMCW interrogator of microstrip antenna for foot pressure sensing," in *Proc. Prog. Electromagn. Res. Symp. (PIERS)*, 2016, pp. 2101–2105, doi: 10.1109/PIERS.2016.7734882.

[35] Z. Yi, L. Xie, S. Xue, and G. Wan, "A passive wireless acceleration sensing system based on patch antenna and FMCW radar," *IEEE Internet Things J.*, vol. 10. no. 12, pp. 10662–10674, Jun. 2023, doi: 10.1109/JIOT.2023.3240027.

[36] *Analysis of Free Vibrations of Tall Buildings*. Accessed: May 12, 2022. [Online]. Available: https://ascelibrary.org/doi/epdf/10.1061/%28ASCE%290733-9399%281994%29120%3A9%281861%29

[37] J. W. Tedesco and T. Krauthammer, *Structural Dynamics*.

[38] *Product Catalog 2022*, Robert Bosch, Gerlingen, Germany, 2022.

Liyu Xie (Member, IEEE) received the B.S. and M.S. degrees in mechanics engineering from Tongji University, Shanghai, China, in 2000 and 2003, respectively, and the Ph.D. degree in system design engineering from Keio University, Tokyo, Japan, in 2009.

Since 2009, he has been with the College of Civil Engineering, Tongji University, where he is currently an Associate Professor. His current research interests include smart sensors, structural health monitoring, and structural vibration control.

Tonghai Wu received the B.S. degree in civil engineering from Tongji University, Shanghai, China, in 2021, where he is currently pursuing the master's degree in civil engineering.

His current research interests include smart sensors for structural health monitoring and smart aggregate.

Zhuoran Yi received the B.S. and M.S. degree in civil engineering from Tongji University, Shanghai, China, in 2018 and 2021, respectively.

His current research interests include smart sensors for structural health monitoring and FMCW-based radio frequency identification (RFID) detection systems.

Xiaoli Fu received the B.S., M.S., and Ph.D. degrees in hydraulic engineering from Wuhan University, Wuhan, China, in 2000, 2003, and 2006, respectively.

She is currently an Associate Professor with the School of Civil Engineering, Tongji University, Shanghai, China. She has more than 15 years of teaching and research experience and has published more than 30 journal articles. Her research interests include environmental hydraulics, computer fluids dynamics, and virtual reality.

Wei Zang received the B.E. degree in applied electronic technology from Shanghai Second Industrial University, Shanghai, China, in 1991.

In 2003, he began working at the State Key Laboratory of Modern Technology for Urban Planning and Design, Tongji University, Shanghai. Since 2010, he has been the Deputy Director of the Office of the Key Laboratory of Ecology and Energy Saving Study of Dense Habitat Ministry of Education, Shanghai. His current research interests include building technology.

Wensheng Lu received the B.S. degree in civil engineering from Zhejiang University, Hangzhou, China, in 1988, and the M.S. and Ph.D. degrees in civil engineering from Tongji University, Shanghai, China, in 1991 and 2011, respectively.

Since 1991, he has been with the College of Civil Engineering, Tongji University, where he is currently a Professor. His current research interests include the seismic testing method of structural and nonstructural components and the safety issues related to building moving technologies.